



Article

Multi-Sensor and Multi-Scale Remote Sensing Approach for Assessing Slope Instability along Transportation Corridors Using Satellites and Uncrewed Aircraft Systems

Marta Zocchi ^{1,*}, Anush Kumar Kasaragod ², Abby Jenkins ³, Chris Cook ³, Richard Dobson ³, Thomas Oommen ², Dana Van Huis ³, Beau Taylor ⁴, Colin Brooks ³, Roberta Marini ¹, Francesco Troiani ¹ and Paolo Mazzanti ^{1,5}

¹ Department of Earth Sciences, Sapienza University of Rome, P.le Aldo Moro 5, 00185 Rome, Italy

² Department of Geological and Mining Engineering and Sciences, Michigan Technological University, Houghton, MI 49931, USA

³ Michigan Tech Research Institute, Michigan Technological University, 3600 Green Ct, STE 100, Ann Arbor, MI 48105, USA

⁴ Colorado Department of Transportation, Denver, CO 80216, USA

⁵ NHAZCA S.r.l., Via Vittorio Bachelet, 12, 00185 Rome, Italy

* Correspondence: marta.zocchi@uniroma1.it

Abstract: Rapid slope instabilities (i.e., rockfalls) involving highway networks in mountainous areas pose a threat to facilities, settlements and life, thus representing a challenge for asset management plans. To identify different morphological expressions of degradation processes that lead to rock mass destabilization, we combined satellite and uncrewed aircraft system (UAS)-based products over two study sites along the State Highway 133 sector near Paonia Reservoir, Colorado (USA). Along with a PS-InSAR analysis covering the 2017–2021 interval, a high-resolution dataset composed of optical, thermal and multi-spectral imagery was systematically acquired during two UAS surveys in September 2021 and June 2022. After a pre-processing step including georeferencing and orthorectification, the final products were processed through object-based multispectral classification and change detection analysis for highlighting moisture or lithological variations and for identifying areas more susceptible to deterioration and detachments at the small and micro-scale. The PS-InSAR analysis, on the other hand, provided multi-temporal information at the catchment scale and assisted in understanding the large-scale morpho-evolution of the displacements. This synergic combination offered a multiscale perspective of the superimposed imprints of denudation and mass-wasting processes occurring on the study site, leading to the detection of evidence and/or early precursors of rock collapses, and effectively supporting asset management maintenance practices.

Keywords: rock slope instabilities; UAS; InSAR; multi-scale; instabilities; early precursors; erosion processes; asset management plan



Citation: Zocchi, M.; Kasaragod, A.K.; Jenkins, A.; Cook, C.; Dobson, R.; Oommen, T.; Van Huis, D.; Taylor, B.; Brooks, C.; Marini, R.; et al. Multi-Sensor and Multi-Scale Remote Sensing Approach for Assessing Slope Instability along Transportation Corridors Using Satellites and Uncrewed Aircraft Systems. *Remote Sens.* **2023**, *15*, 3016. <https://doi.org/10.3390/rs15123016>

Academic Editor: Anna Giacomini

Received: 28 April 2023

Revised: 5 June 2023

Accepted: 7 June 2023

Published: 9 June 2023



Copyright: © 2023 by the authors. Licensee MDPI, Basel, Switzerland. This article is an open access article distributed under the terms and conditions of the Creative Commons Attribution (CC BY) license (<https://creativecommons.org/licenses/by/4.0/>).

1. Introduction

Slope instabilities, especially along transportation corridors in mountainous areas, pose a threat to facilities, settlements and life [1,2]. According to the United States Geological Survey (USGS), the destruction caused due to landslides, in general, results in 25 to 50 deaths per year and costs in excess of USD 1 billion in damages in the United States alone [3]. With the increasing population and demand for advanced infrastructure, it is crucial to assess mass-wasting hazards and manage the associated risks for maintaining transportation corridor safety [4,5]. Among the recurrent mass movements involving highway networks, rockfalls are among the most hazardous types. Despite the often limited volumes of rockfalls, their high energy and velocity, as well as their frequency, make them a major cause of mass-wasting fatalities [6–8]. Several geomorphic processes (including

thermic cycles, progressive weathering of rock materials and water infiltration) control the mechanical properties and the degradation state of the rock mass, therefore influencing its overall stability [7,9,10].

Conventional methods of rockfall hazard assessment involve rigorous fieldwork where quantitative measurements (e.g., spacing, density and orientation of fractures) and qualitative evaluations (e.g., recent detachments and potential sources of future failures) are addressed [5]. Although these in situ point measurements can effectively assist the prediction of slope stability with high precision, they are time-consuming, have limited spatial extent, and can be expensive. Unprecedented opportunities derive from the extensive use of remote sensing methods, which facilitate an efficient, cost-effective and safe assessment of the slope pre-failure conditions. Remote-sensing-based data come in a wide range of platforms (e.g., spaceborne and airborne) and spatio-temporal and radiometric resolutions [11]. At a large scale, satellite synthetic aperture radar interferometry (InSAR) enables the precise monitoring of ground deformations over tens of square kilometers. InSAR analysis thus represents one of the best instruments for creating regional-scale slope instability inventories [12,13] and relative susceptibility maps [14,15]. However, due to the line-of-sight acquisition mode of the satellite sensors, geometric distortions like shadowing effects may limit the capacity of this method to effectively investigate vertical slopes. Recent developments in uncrewed aircraft systems (UASs) include their abilities to carry multiple sensors, fly on demand, orient the sensor's look angle based on the topography characteristics, and achieve ultra-high-resolution information (1–20 cm) for precise morphodynamic characterization of processes and landforms [16]. These practical advantages are optimal for rock mass stability evaluation, and were successfully exploited by previous studies through classification systems such as the slope and rock mass rating [17–19]; realization of tridimensional models for mapping geomechanical properties [20–23] or for stability analysis, hazard and risk modeling [24–28]; exploitation of multispectral and hyperspectral sensors for landslide susceptibility assessment; and detailed analysis of slopes' lithological and moisture conditions [29–31]. In particular, the scientific community is dedicating its efforts to identifying early precursor signals indicative of instability events or studying the temporal morphoevolution of block and debris detachments, exploiting topographic models and quantitative geomechanical characterization of the rock masses. Progressive creep, deformation and micro-tremors are clear indicators of the ongoing disruption of the slope stability, therefore they are the primary goals for a comprehensive assessment of rockfall hazard. Most of the previous literature so far lies with the application of terrestrial-based technologies, such as terrestrial laser scanners (TLS) [32–36] or terrestrial InSAR platforms (TInSAR) [37,38] to identify pre-failure information. Despite the numerous advantages and exceptional precision of these techniques, however, several challenges arise due to the high costs and logistical constraints (linked to the positioning of the instrumentation and the lack of data in shaded areas). The versatility of UAS sensors and platforms renders them an efficient (yet far from being fully exploited) alternative for evaluating the early precursors of rock destabilization through topographic models [39]. Refs [40–43] analyzed the predominant discontinuities through UAS-based structure-from-motion (SfM) photogrammetry techniques to estimate average block sizes and determine their simulated run-out. A multi-scale approach consisting of the creation of different digital surface models of the slope along a road was adopted by [44]. Statistically representative geometrical data for the discontinuities of the rock mass were obtained to eventually define the possible kinematic mechanisms and volumes of potentially detachable blocks. To determine potentially unstable rock volumes and provide the magnitude of future rockfalls, geometrical and geomechanical properties of the main sets of discontinuities and joints of the rock mass were extracted by [45,46], respectively, using photogrammetry point clouds alone or a combination of thermal images and a photogrammetric cliff model. These applications, however, are limited to accounting for the discontinuities' properties as the sole factor influencing the slope stability, disregarding the progressive alteration and fragmentation driven by water infiltration and erosion. In this framework, our study represents one of the

few applications of UASs for detecting local to micromorphological signatures of the initial stages of slope disruption. Furthermore, we consider the multiscale imprint of denudation and mass-wasting processes, along with their respective preliminary indicators, exploiting a synergic combination of satellite and drone-based data to obtain an in-depth characterization of landforms and processes [47–50]. In this study, the morphological features and radiometric differences associated with significant change detection over the study area are investigated. We apply a multiscale and multisensor approach integrating satellite-based InSAR analysis with UAS-based data to assess mass-wasting processes on two study sites located along State Highway 133 near Paonia Reservoir in Colorado, USA.

2. Geographical and Geological Settings

The Paonia Reservoir area is part of the southern sector of the Piceance Basin, a structural and sedimentary basin formed during the late Cretaceous–Paleocene Laramide orogeny. The exposed stratigraphic sequence, representing this Cretaceous–Tertiary boundary, mainly consists of the white rocks of the Ohio Creek Member and the variegated rocks of the Wasatch Formation (Figure 1), both deposited in a non-marine environment. The first unit was considered by many stratigraphers as a separate formation because of its distinctive white/light-gray color but was eventually reduced in rank to the Ohio Creek Member of the Mesaverde Group by [51], who described it as a deep paleo-weathered kaolinitic zone undistinguishable in age (late Cretaceous) from the underlying rocks of the Mesaverde group. The lithological composition varies from light-gray or white conglomeratic sandstone with well-rounded chert pebbles in the lower and upper part, to interbedded layers of sandstone, siltstone and shale with some thin coal lenses in the middle sector [51–53]. This lithological alternation finds expression in slope morphology, where thick and resistant sandstone ridges intermingle with more erodible siltstone and shale layers. The white-weathering Ohio Creek member is unconformably overlain by lower Cenozoic rocks of the Wasatch Formation. At this location, the Wasatch Formation deposition is characterized by non-kaolinized, mottled maroon medium- to coarse-grained conglomeratic sandstones [51–53].

The area of interest referred to as Paonia 1A is located along the western side of Paonia Reservoir and around 500 m north of Paonia Dam (from MP 24.7 and 25.0 of State Highway 133, Figure 1). The slope reaches the highest values of steepness (up to 65°) along the upper part, where the bedrock unit of the Mesaverde Group outcrops. In this part, light brown and light tan sandstone beds (a few meters thick) are interbedded with thinner gray mudstone and shale layers, corresponding to the Barren Member of the Mesaverde Group (Figure 1) [54]. The lowest part of the slope, with a mean steepness value around 35–40°, is mainly composed of an unconsolidated deposit fed by mass wasting due to the mechanical and chemical weathering of the bedrock outcropping in the upper part. The resulting scree slope is constituted by small-sized rocks (a few cubic centimeters). At the same time, massive boulders are more likely to accumulate along the foot of the slope and inside the roadside ditch.

The second area of interest (hereafter called Paonia 1B) is located two miles north of Paonia Reservoir on the west side of SH133 (from MP 29.9 to 30.2), just north of the confluence of West Muddy Creek into East Muddy Creek and along the south-eastern slope of the Bull Mountain (Figure 1). This sector of SH133 aligns with the foot of a slope characterized by a mean steepness value of about 40°, sharply interrupted by a flatter area (less than 10°) located in its middle portion. A concave-shaped landslide scar isolates several morphological steps in the northern sector of the area, which could be kinematically due to the roto-translational landslide mechanism.

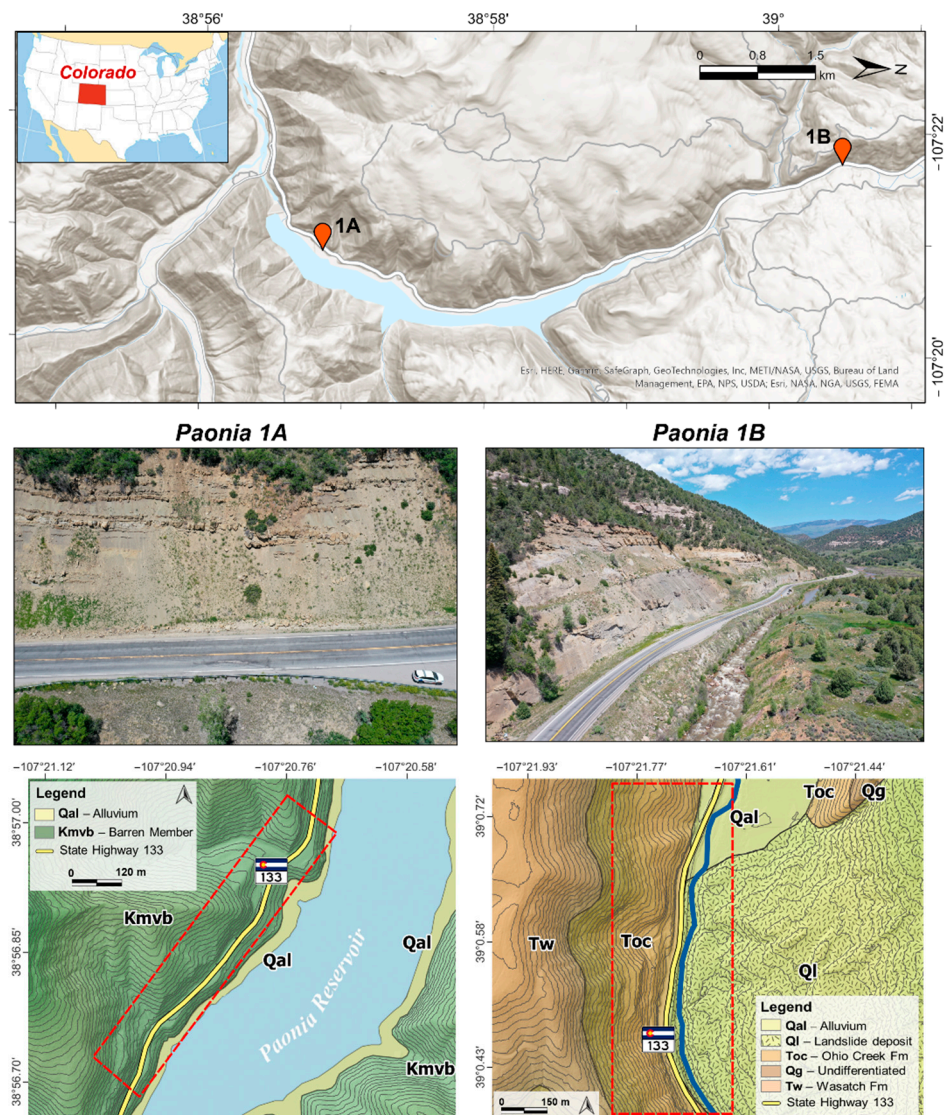


Figure 1. Location of the study areas along State Highway 133 (upper panel). The oblique view of the slopes of interest and their geological setting is reported in the bottom panels, respectively for Paonia 1A (left panels) and Paonia 1B (right panels). The figures were realized using ArcGIS Pro 3.0.4 and QGIS 3.22.14.

3. Materials and Methods

This section includes two main subsections, for the interferometric synthetic aperture radar analysis (InSAR) and the UAS-based acquisition and processing techniques adopted in the present work. The first analysis was performed at the catchment scale: the scope was detecting large deformation processes and considering their interaction on portions of SH133 wider than those included in the actual study areas. Downscaling the investigation, the UAS-based products were used to identify signs of slope instabilities at the small and micro-scale. In particular, different radiometric sensors (i.e., optical, thermal and multispectral) were combined to highlight morphological variations related to erosion or accumulation processes.

3.1. Satellite-Based (InSAR) Analysis

Advanced differential interferometric synthetic aperture radar (A-DInSAR) is a multi-image process that provides high-resolution measurements over large areas [55]. Specifically, the persistent scatterers (PS) technique [56] is capable of identifying and measuring the displacement of millions of ground points, thereby providing a much more detailed

and comprehensive understanding of ground deformation (and its association with geological processes) over time. PSs represent the time-coherent pixels retrieved in the stack of differential interferograms, thus corresponding to phase-stable objects in the scene [57]. For the present study, medium-resolution Sentinel-1 data were used for the 2017–2021 time interval. The European Space Agency’s two-satellite constellation has the main advantage of high temporal coverage (revisit time of up to 6 days) over the same area. The dataset was analyzed in the SARPROZ software 2022 (the SAR processing tool by Perez [58] and allowed to estimate both the average line-of-sight (LOS) velocity and the displacement time series (TS) for the PS over the two study areas. The essential steps of the processing consist of co-registering all of the images to the one chosen as the master. Subsequently, two radar parameter maps are generated to estimate the quality of the persistent scatterer candidates (PSCs): these maps respectively represent the multi-temporal amplitude value for each pixel (reflectivity map) and the coefficient of the amplitude variation (amplitude stability index map). The next step relates to the detection and removal of the atmospheric phase screen (APS) for estimating each persistent scatterer (PS) and the velocity values along the line-of-sight (LOS) relative to a reference point identified in a stable region [59,60]. At the end of the PSI workflow, PSs having a low temporal coherence threshold (<0.5) were discarded. Of the two available orbital geometries, only the results from the ascending geometry analysis were reliable enough to be interpreted. Geometric distortions due to the off-nadir angle of the descending geometry, in particular shadow effects, heavily affected the spatial coverage of the data.

3.2. UAS-Based Acquisition and Processing

The multi-temporal UAS-based data acquisition aimed to create high-resolution products to assess a comprehensive deterioration model of the rock mass, including seasonal moisture condition variations, structural changes and lithological characterization. For this purpose, two UAS flight campaigns were carried out in September 2021 and June 2022; the flights were operated from traffic pullouts along Colorado SH133 (Figure 2a) in adherence to Federal Aviation Administration (FAA) regulations regarding drone visual-line-of-sight (VLOS), maximum flight altitude relative to ground level, and flights over traffic. Moreover, visual observers selected from the field team helped UAS pilots ensure air space safety.



Figure 2. Examples of drones, instruments and sensors used during the field operations. Panel (a) Bergen Hexacopter flying over Paonia 1B site; (b) AeroPoint and Trimble 3 GPS unit placed at Paonia 1A site; (c) Tetracam multispectral camera; (d) Dual optical and thermal cameras.

To accurately georeference drone-derived image products, together with cloth photogrammetry targets, we placed ten ground control targets (Figure 2b) throughout the planned study area. Each AeroPoint already includes built-in GNSS and Wi-Fi systems that allow a level of accuracy of down to 3 cm during the imagery georeferencing process. The flights were planned with overlaps of 70% along the flight line and 60% at the sides and were manually carried out at the same time of the day to cover the study sites under similar lighting conditions each year. A set of multi-sensor cameras were flown as payload on three different UASs to capture and analyze complementary and interconnected environmental conditions that contribute to the rock instabilities of the area. More than ten flights per survey were necessary to acquire nadir and oblique-oriented images to represent the near-vertical slopes accurately. The Tetracam multispectral camera (Figure 2c) was flown as payload on the Bergen Hexacopter at each study site. This sensor can capture detailed information about the spectral characteristics of the landscape, which can reveal potential changes in moisture content and mineral composition.

The M2EA (Figure 2d), equipped with dual optical thermal integrated cameras, was used to capture radiometrically calibrated thermal imagery over each site. In Table 1, we summarize both the drones' specifications and the type of sensors flown as payload.

Table 1. The characteristics of the drones used for the study.

Characteristics	DJI Mavic 2 Pro	DJI M2EA	Bergen Hexacopter
Camera	Integrated 20 MP	Integrated dual optical (12/48 MP) thermal (640 × 480 radiometric 30 Hz)	Tetracam Micro-MCA6
Maximum take-off weight (kg)	0.907	0.11	4.5
Flight range (min)	25	25	15
Flight altitude (m)	45–60	30–60	30–70
Maximum horizontal speed (km/h)	72	72	30
N° of images (nadir)	2000	3500 thermal	Tetracam: 700 (6 bands)
N° of images (oblique)	800	900 thermal	Tetracam: 500 (6 bands)

3.2.1. Pre-Processing

Prior to drone flights, the ground control, in the form of cloth photogrammetry targets and AeroPoints, were evenly placed throughout the planned study area (Figure 2b). The AeroPoints continuously logged their position while the cloth photogrammetry targets were surveyed using a Trimble 3 GPS unit, with both methods providing coordinates with centimeter-level accuracy. These ground control targets, appearing within the field of view of the drone camera, provided geolocation information for accurately positioning the drone-based orthoimage products.

For the optical imagery collected by the DJI Mavic 2 Pro, the software Agisoft Metashape v.1.8.1 was used to align and find tie points between photos, producing image-based dense clouds, orthophotos, and DEMs. Ground control position information collected for each target was required for this processing to produce accurately geolocated products.

For the thermal imagery collected by the DJI M2EA, the raw images were processed into per-pixel true-temperature radiometric images using AethaGlobal's ThermoConverter software v.1.3.14.0. The true-temperature images were then processed into a true-temperature orthophoto using the image processing software Pix4Dmapper v.4.7.5. The orthophoto was geo-referenced using the ground control present in the orthoimage.

For the 6-band multispectral imagery collected by the Tetracam Micro-MCA6, raw images were processed using Tetracam's proprietary 'PixelWrench2' software v.1.2.4.9 to convert raw images into multi-band tiff images. The tiff images were then more precisely aligned using intensity-based image registration techniques available within MATLAB. The resulting aligned images were then processed using Agisoft Metashape to create a 6-band orthoimage for the study site. Ground control target GPS data were used as inputs during Metashape photogrammetry processing to create a georeferenced product.

3.2.2. Processing: Classification Analysis

The georeferenced 6-band Tetracam orthoimage was classified into several soil or rock types (e.g., sandstone, arkosic sandstone), vegetation (i.e., living or dead), and other classes (e.g., shadows, road) using the software Trimble eCognition v.10.3 [61]. To create this classification, the orthoimage was first segmented in eCognition using a multiresolution segmentation best-fitting neighbor algorithm that groups pixels into objects by minimizing or optimizing the average heterogeneity of image objects [61]. In this process, pixels were grouped into segments based on the spatial and spectral characteristics of the pixels and their neighbors, using all six bands of the Tetracam orthoimage. Desired mean segment size parameters were input by the user to affect the number of segments, the size of segments (which impacts the final classification), and the file size of the segmented image. Segmenting the image allowed the user to perform object-based image analysis (OBIA), which can be an improvement over pixel-based image classification for representing landscapes [62]. Pixel-based image classification solely uses the spectral information of the image bands in the classification. Grouping these pixels into objects using multi-resolution segmentation created an object-based classification that was based on both the spectral and spatial characteristics of the 6-band orthoimage. After the image was segmented, a supervised classification hierarchy was created, containing the distinct mapping classes. Based on observations made in the field (ground truth information), and visual observations of the image itself, the eCognition user then assigned individual segments as samples to each desired class in their class hierarchy. The user might use both ground-truth information and their own visual observations of the orthoimage to discern different vegetation types and assign samples to unique vegetation classes (e.g., living and dead vegetation classes). After some samples were assigned to each class in the class hierarchy, the analyst then used a nearest neighbour classification algorithm [61] to assign each image object (segment) in the image membership to a class based on the spectral information of the samples. The classified orthoimage was then exported in a geotiff format to be interpreted in a GIS environment together with other analyses.

3.2.3. Processing: Change Detection Analysis

Change detection techniques involve the comparison of multi-temporal datasets to assess the temporal effects of a specific process and quantify changes due to natural phenomena or anthropogenic activities [63]. Significant changes identified between at least two images lead to the generation of a change map. [64] provided a comprehensive review of different change detection techniques, addressing issues and challenges of performing change detection on remotely acquired images. For this study, the algebra-based change detection approach was followed, which consists of the application of mathematical operation on each pixel to retrieve the difference image. The DEM generated using the orthoimages from the 2021 and 2022 data collection, after preprocessing, were coregistered and the algebraic operation of subtraction was performed on them in ArcGIS Pro 3.0.1. The 2022 image was subtracted from the 2021 image to monitor changes that occurred after the 2021 data collection. The differences that were reflected after the change detection task were mostly due to elevation changes between the two acquisitions.

While the DEM comparison allowed the extraction of information related to changes in elevation, the orthoimages acquired from the Mavic 2 Pro were processed to assess any variation in terms of radiometric characteristics.

The change detection analysis that was implemented on IRIS software v.23.0, developed by NHAZCA S.r.l. [65], involves the use of the Structure Similarity Index Method (SSIM) algorithm [66], a function of the brightness, contrast and structural component of pixels and determined by constructing a moving window around each pixel for both images. The SSIM is defined as follows:

$$SSIM(x, y) = \frac{(2\mu_x\mu_y + C_1)(2\sigma_{xy} + C_2)}{(\mu_x^2 + \mu_y^2 + C_1)(\sigma_x^2 + \sigma_y^2 + C_2)} \quad (1)$$

where μ_x and μ_y represent the luminance for the two image signals, σ represents the contrast and C represents a constant to ensure stability when the denominator is very close to zero.

This equality index represents the radiometric variation between the image selected as the master (i.e., 2021 orthoimage) and the one selected as the slave (i.e., 2022 orthoimage) on a scale from 0 to 1 [67]. The closer the index is to 1, the more the two images are similar: an index equal to 1 means that no changes were identified over the observed time interval [68].

4. Results

This section summarizes the results obtained through the PS-InSAR analysis, visual interpretation of UAS-based products, and the classification and change detection analyses carried out on them. The results were divided into two subsections for Paonia 1A and Paonia 1B, respectively.

4.1. Paonia 1A

Regarding the UAS-based analysis, it has been decided to present the primary outcomes of two specific sectors that are representative of the processes observed throughout the entire area of interest. These sectors, shown in Figure 3, are located along SH133 in the central part of the study area. Sector I stretches nearly to the northern boundary of the slope of interest: Figure 4 illustrates the same area in different panes, each representing a specific analysis carried out on the site of interest. As evident from the orthophoto captured through the DJI Mavic 2 Pro optical sensor (Figure 4a) in June 2022, the slope appears almost entirely uniform, with sedimentary rocks in a tan shade and dotted with patches of vegetation in the central part. However, a linear pattern of slightly lighter color can be observed in the upper part of the slope, corresponding to the exposed rock strata.

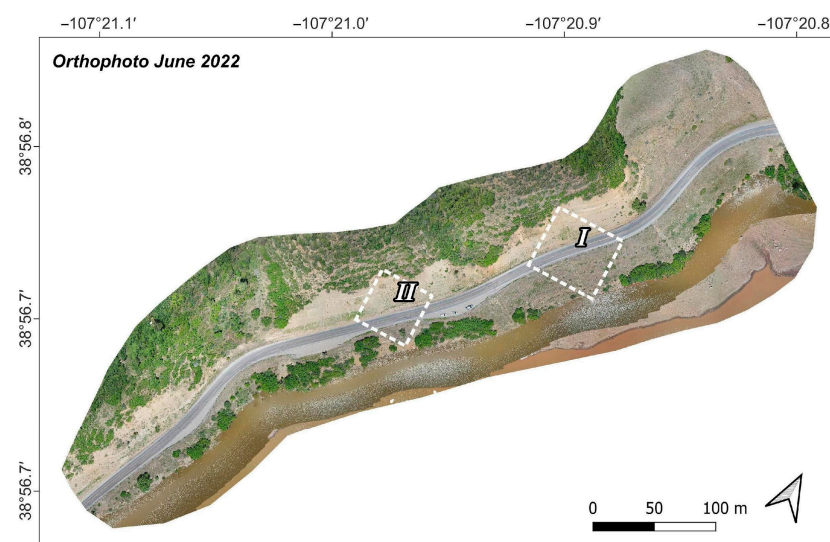


Figure 3. Location of the two most representative Sectors for Paonia 1A study site, respectively referred to as Sector I and Sector II. The figure was realized using QGIS 3.22.14.

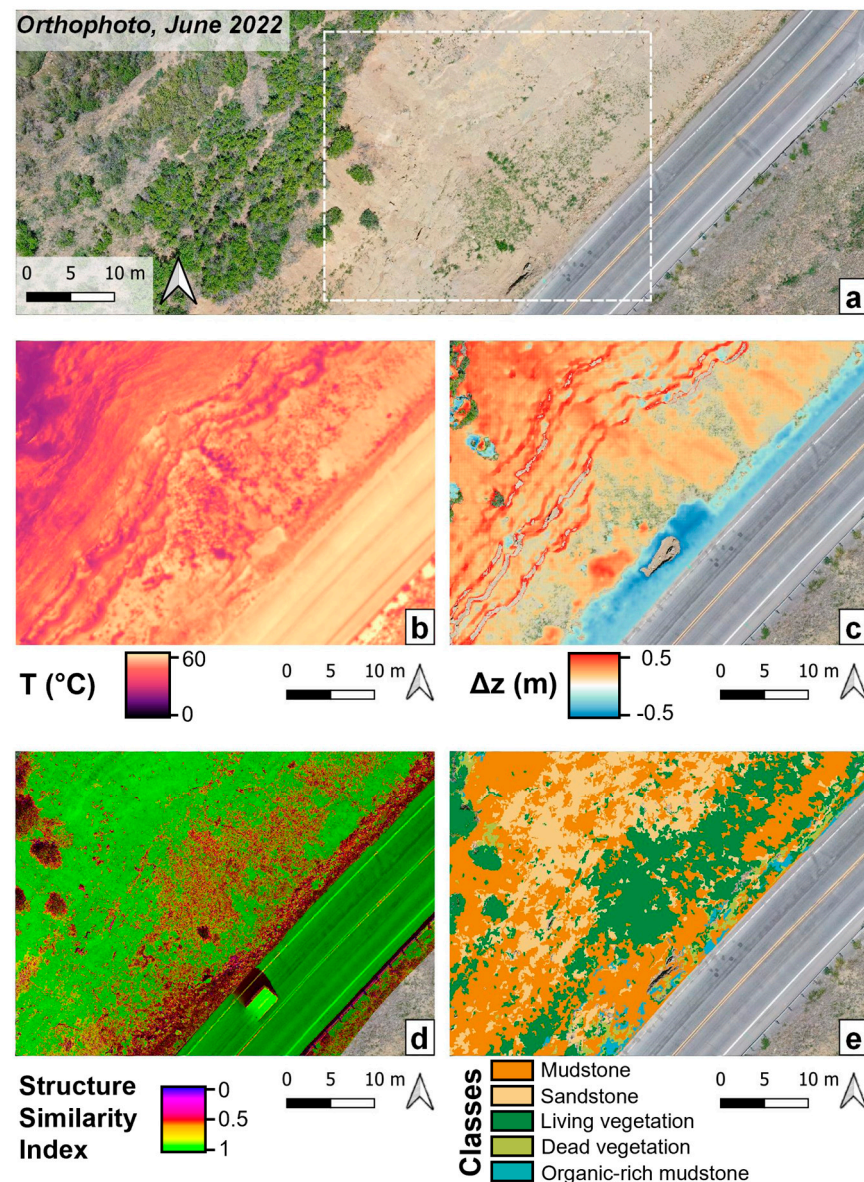


Figure 4. The results obtained for Sector I of the Paonia 1A study area are presented in 5 panels, corresponding to: (a) orthophoto acquired in 2022; (b) per-pixel temperature thermal image; (c) DEM-based change detection; (d) optical-imagery-based change detection; and (e) classes resulting from the classification analysis. The figures were realized using QGIS 3.22.14.

On the contrary, the per-pixel temperature visualization of the thermal image returns improved discrimination of the slope, enabling the identification of distinct patterns and textures distinguished by varying temperature values (Figure 4b). The slope region near SH133 shows the highest temperature values, with an average of around 50 °C. This area becomes more homogenous heading north, while the southern and central portions of the sector exhibit a more granular texture and colder temperatures, which drop by up to 32–33 °C. Particularly in the central part, the slope continuity is interrupted by clusters of lighter color that match the vegetation already identified in the orthophoto. The summit section of the slope, which has a finer texture, displays uniformly distributed temperatures with an average of 45 °C. A distinct central band separates the two regions, which features a linear pattern with alternating areas of cooler temperatures (around 38 °C) and warmer temperatures (around 55 °C), characterized by a coarse texture.

Figure 4c represents the outcome of the DEM-based change detection between the two data collections in September 2021 and June 2022. The elevation difference is represented

with a red-to-blue color scale, where shades of red represent positive values (≥ 0.15 m) while shades of blue represent negative values (≤ 0.15 m). Areas showing negligible or no changes were left uncolored for better interpretability of results. Except for the portion along the roadside, showing an evident decrease, a rise in elevation values between the two years is registered throughout the slope. The values indicating an elevation increase of around 30–40 cm appear to form fan-like shapes, which align along the lower section of the slope and are separated from each other by areas exhibiting minimal variation in height.

For the change detection analysis performed between the orthophotos, choosing a four-pixel window size emphasized even slight radiometric variations. The major part of the scene depicted in Figure 4d has an SSI value close to one, indicating that the 2021 and 2022 images look very similar in terms of radiometric characteristics. The most notable changes are concentrated in the basal and central regions of the slope, where a decrease in SSI (around 0.5) values corresponds with changes in debris accumulation (especially along the roadside) and vegetation presence, the latter of which has a significant impact on the analysis.

The final panel of Figure 4 displays the results of the multispectral image classification. In Sector I, the classification analysis has identified five distinct classes, two of which correspond to the vegetation present in the scene (distinguished as living or dead), while the other three relate to the sedimentological properties of the rocks. These three classes correspond to samples of sandstone and mudstone (with lower or higher organic matter content) that were recognized during the field operations and used as training data.

However, the most representative classes in this area are only sandstone, mudstone, and living vegetation, whereas small scattered patches of dead vegetation and organic-rich debris constitute a minimum part of the scene. The debris accumulation, mainly composed of mudstone, develops along the foot of the slope and on the sandstone bedding plane, whose heads (in beige) are well recognizable in the summit portion.

The same comparative criterion adopted for Sector I is also applied to the results for Sector II, reported in the subsequent panels of Figure 5 to facilitate the visual interpretation of the data. In this case, as well, the sandstone banks that appear in the optical image (Figure 5a) in a slightly lighter shade of beige than the rest of the outcrop emerge clearly in the thermal visualization (Figure 5b), being marked by lower temperature values (around 40 °C) than the sediments (more than 50 °C). The classification analysis validates this finding by clearly differentiating the beige, linear pattern of the sandstone from the more diffused brown of the mudstone, enabling the recognition of the sandstone stratification throughout the entire extent of the scene (Figure 5f). Below these banks, there is a distinct area with sporadic bushes and vegetated spots that can be easily identified through both optical image and object-based classification (Figure 5a,f). These areas correspond to the living vegetation class.

The results of thermal and change detection also confirm the presence of these areas, where the thermal image highlights cooler and potentially more moist zones with temperatures below 40 °C (Figure 5b), while the change detection analysis (Figure 5d) yields an SSI value of 0.5, indicating significant changes over the two years. It is worth noting that the variations detected in the change detection analysis do not exhibit a chaotic structure like the one shown in Figure 4d, but rather present a linear pattern that converges towards the base of the slope. Moreover, subtle changes in the fractures constituting a semicircular road crack, located right below the convergent linear pattern, were highlighted by the analysis.

Similarly to Sector I, the DEM-based change detection for Sector II reveals a significant material accretion near the road edge. Besides the uniform accumulation of debris in this region (15–30 cm), large blocks, which are predominantly sandstone blocks (Figure 5f), can be also found near the road pitch.

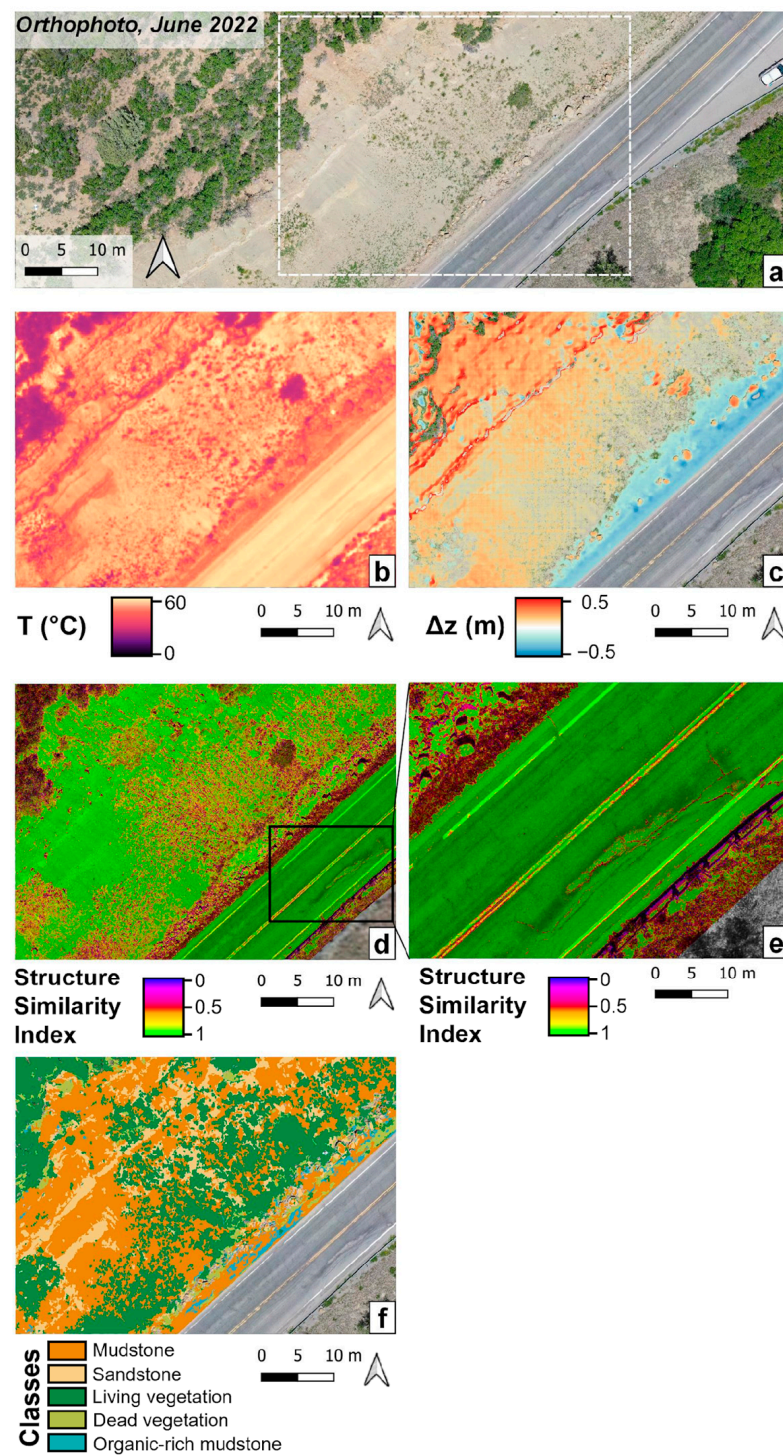


Figure 5. The results obtained for Sector II of the Paonia 1A study area are presented in 6 panels, corresponding to: (a) orthophoto acquired in 2022; (b) per-pixel temperature thermal image; (c) DEM-based change detection; (d,e) optical-imagery-based change detection at various scales and (f) classes resulting from the multispectral classification analysis. The figures were realized using QGIS 3.22.14.

For the Paonia 1A site of interest, the results of the PS-InSAR analysis show a few sparse measurement points, which are not representative of significant deformations affecting the slope.

4.2. Paonia 1B

The PS analysis allowed us to investigate the deformations occurring on the slope of interest at Paonia 1B, considering its morphoevolution on a larger scale. The measurement points, derived from 250-km-wide imagery (i.e., interferometric wide swath, *IW*), cover the slopes that develop along the hydrographic right and left banks of East Muddy Creek. Average velocities ranging from -4 to -10 mm/y were recorded in the southernmost part of the slope of interest, forming a small deformation cluster moving away from the sensor and thus indicating a downslope movement (Figure 6a). On the opposite slope, apart from a stable PS cluster located along the foothill, a clear movement with displacement rates of over 4 mm/year is measured towards the east direction (Figure 6b). The analysis provided important clues to the recent displacement rates of a landslide phenomenon already well identified in the historical maps of the area [52,69], but whose state of activity was investigated only by [70]. This landslide is part of the broader “East Muddy Creek Landslide Complex”, which consists of three distinct phenomena located on the western flank of the Ragged Mountains and that was mapped through the visual interpretation of the one-meter LiDAR-based DEM produced within the framework of the 3D Elevation Program (3DEP) [71] and the PS-InSAR results.

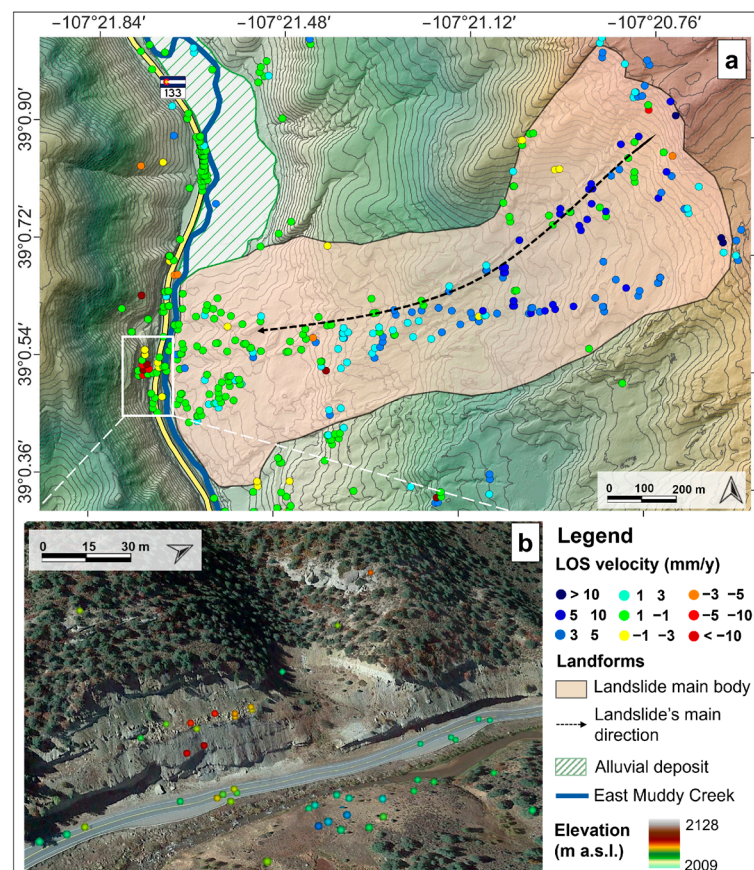


Figure 6. PS-InSAR results for Paonia 1B site. In the upper panel (a) the catchment scale ground deformations are shown. The massive landslide phenomenon retrieved by the PS-InSAR analysis displays displacement rates of up to 10 mm/year. At a smaller scale (panel (b)), a well distinct cluster with 3–10 mm/year displacement rates is visible on the opposite bank. The figures were realized using QGIS 3.22.14.

Similarly to Paonia 1A, distinctive sectors of Paonia 1B (Figure 7) were chosen to represent landforms and processes occurring on the slope. Sector I covers the left flank of the concave-shaped landslide scar which interrupts the continuity of the strata. A massive sandstone bank, lighter in color, bounds a flat area where grayish and brownish debris

accumulates (Figure 8a). A more detailed differentiation of the slope features is captured by thermal (Figure 8b) and multispectral sensors (Figure 8c).

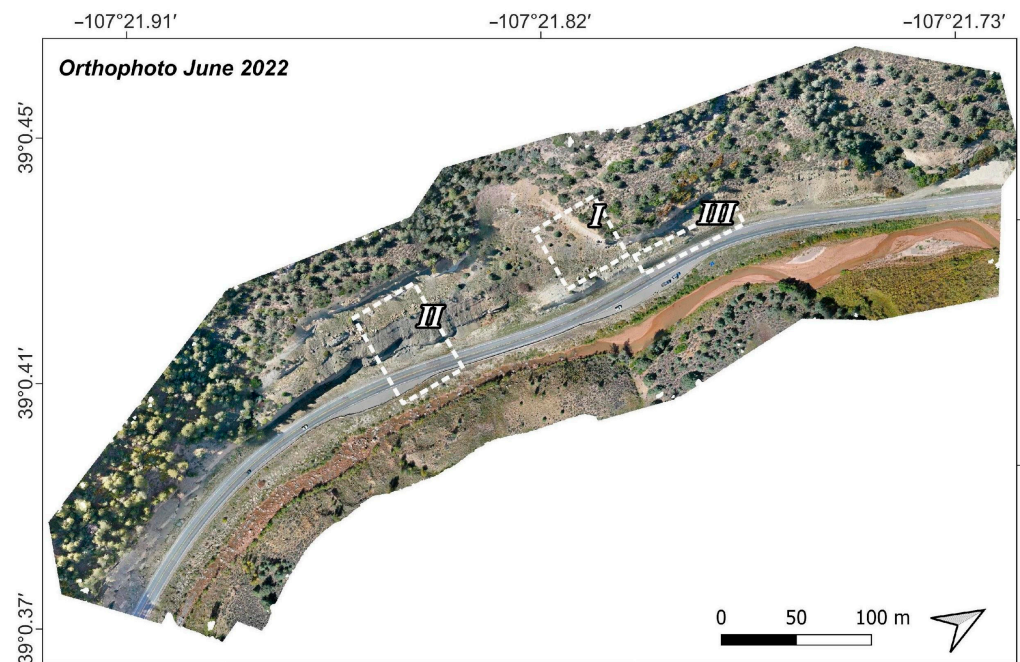


Figure 7. Location of the three most representative Sectors for Paonia 1B study site, respectively referred to as Sector I, II and III. The figure was realized using QGIS 3.22.14.

The overhanging sandstone bank is still well distinguished from the surroundings in terms of lower temperature, appearing as a continuous red/purple band and dividing the vegetated top of the slope from the warmer soil and debris area (temperature up to 50 °C). Just below the sandstone outcrop, the multispectral classification identifies shotcrete covering the slope, contrasted by sandstone's higher temperature values and the unconsolidated material's lower values. Scattered features, corresponding to low-growing vegetation (dead and living) and trees, allineate along the eastern section of the slope, while the mudstone class is found in its central area. The radiometric change detection highlights significant changes ($SSIM < 0.5$, Figure 8d), mostly in correspondence with the vegetated spots but, where the mudstone class outcrops, a linear pattern with similar low values of SSIM is also identified, developing along the steepest part of the central area. Figure 8e focuses on the aforementioned linear pattern, clearly visible between the vegetation.

Sector II is located slightly to the south and includes a portion of a stepped slope, where vertical sandstone strata alternate with erodible layers, forming gentler morphologies. Few reliable persistent scatterers, in the upper part of the slope and specifically on the less steep portions (Figure 9a), recorded an average velocity of up to 10 mm per year in the LOS direction (i.e., downslope). The thermal visualization of the scene shows quite similar temperature values ranging between 42 and 50 °C (Figure 9b). The only exceptions are represented by the lower temperatures of the vertical slope faces and three warmer spots (more than 55 °C) along the roadside. The two yellow spots located in the northern part of the scene present a fan-shaped morphology, with the apex in the vicinity of the vertical road cut, whereas the third one is more distributed. In the last panel of Figure 9, the DEM-based change detection outcomes are shown.

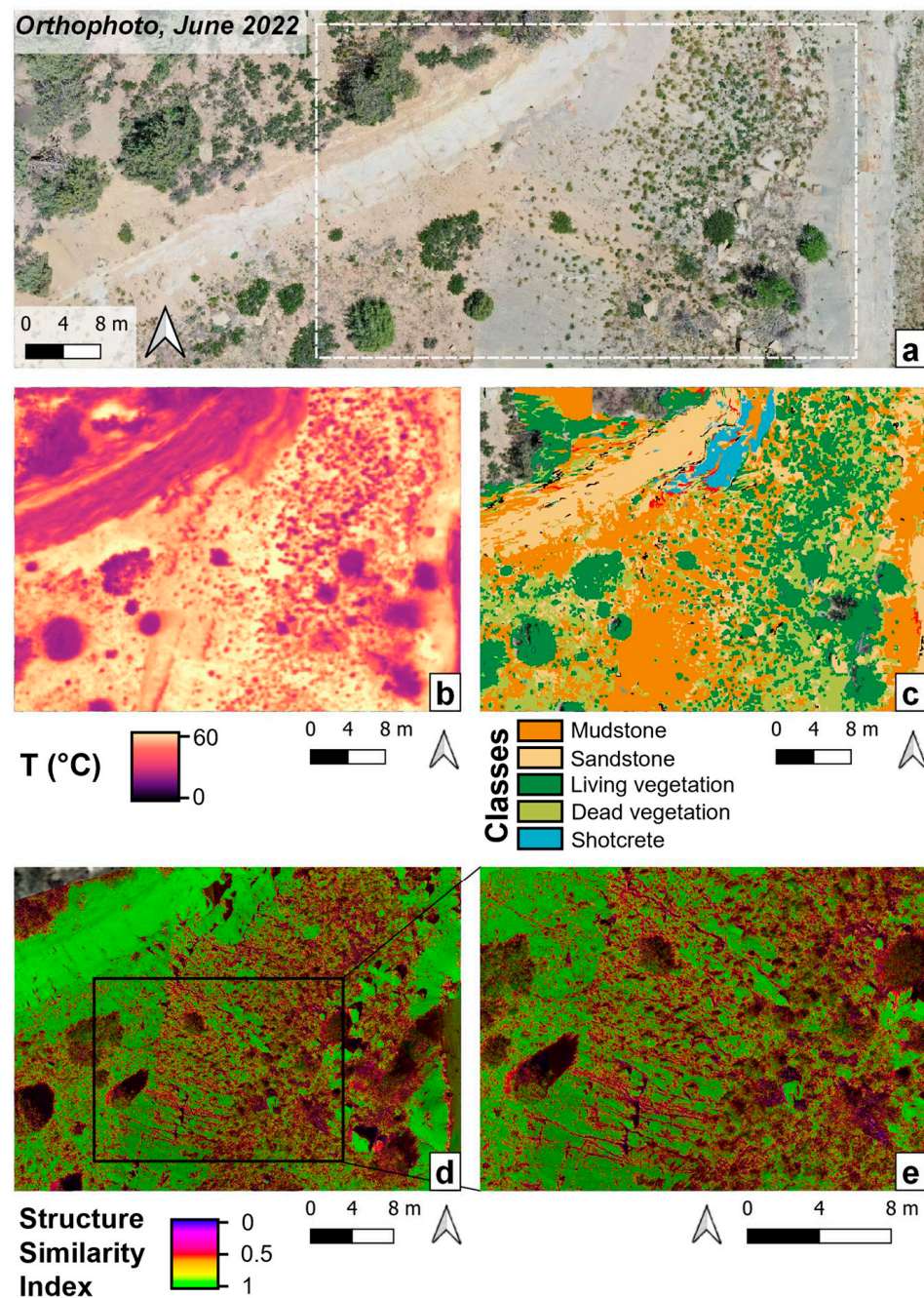


Figure 8. The results obtained for Sector I of the Paonia 1B study area are presented in 5 panels, corresponding to: (a) orthophoto acquired in 2022; (b) per-pixel temperature thermal image; (c) classes resulting from the classification analysis; (d,e) optical-imagery-based change detection at various scales. The figures were realized using QGIS 3.22.14.

A diffuse increase of about 30 cm in height matches the fan-shaped spot in the northern part, with very limited incrementations of more than 50 cm along its boundaries. A sharp change in elevation values can be also noticed in the central part of the scene, where two adjacent areas show differential movements in opposite directions (blue and red areas in Figure 9c): in both cases, the elevation change reaches 50 cm.

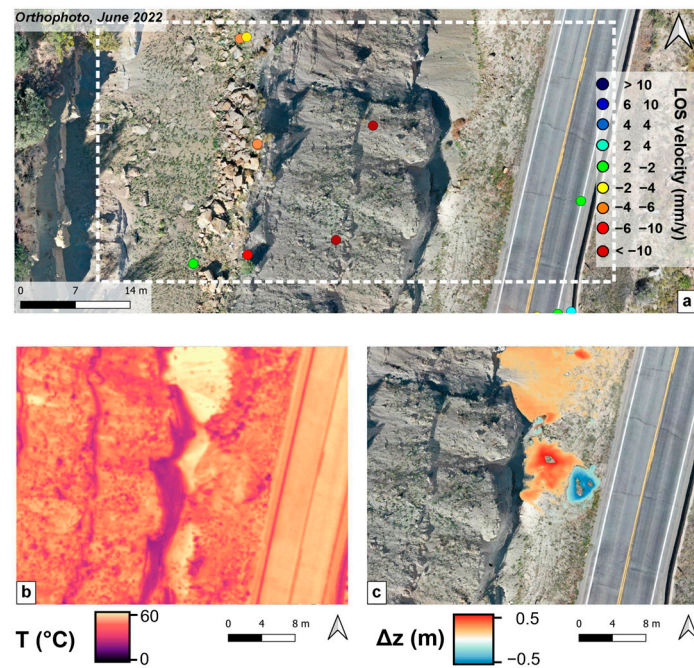


Figure 9. The results obtained for Sector II of the Paonia 1B study area are presented in 3 panels, corresponding to: (a) orthophoto acquired in 2022 and PS-InSAR analysis; (b) per-pixel temperature thermal image; (c) DEM-based change detection.

The third and last sector analyzed for the Paonia 1B area was chosen to represent the analysis carried out on a vertical surface like a road cut. In the orthophoto (upper panel of Figure 10) the surface predominantly appears in two shades of grayish beige. The darker shade is predominant on a small portion on the left and in the upper part of the cut, while the lighter shade of beige is along the base and at the edges of the image. This slight color difference is, on the contrary, well perceivable in the multispectral classification (Figure 10, lower panel), and respectively corresponds to the Sandstone (blue) and Weathered Sandstone (yellow) classes.

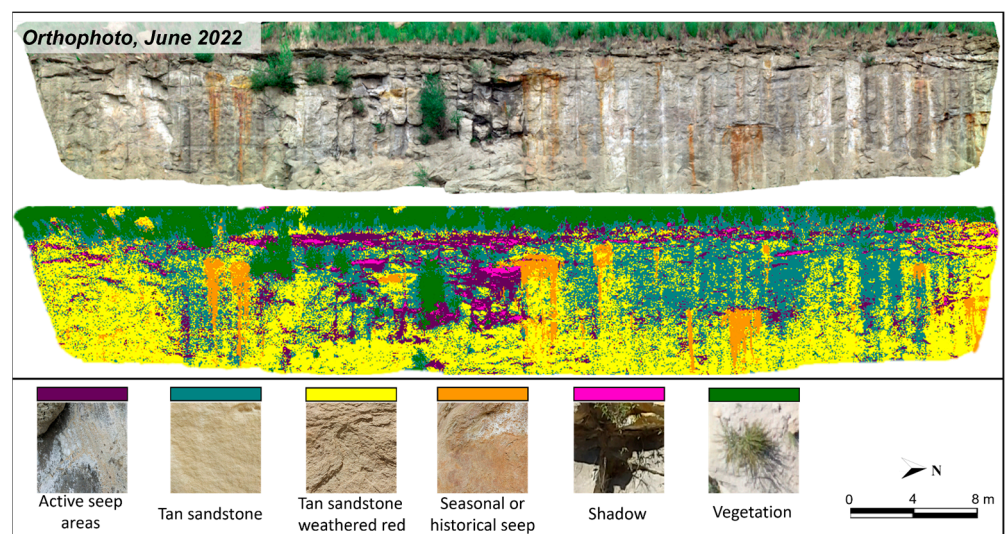


Figure 10. Sector III: multispectral image classification of the road cut. The figures were realized using QGIS 3.22.14.

A definite purple layer is interpreted as an area of active seep that stretches right under the vegetation covering the top of the surface and can also be found in the central

part of the outcrop, along with minor shadowed areas. Inactive seep areas, corresponding to the orange vertically elongated features in the orthophoto, perfectly match the orange category of the classification analysis.

5. Discussion

This study aims to examine the ability of different sensors to identify evidence and early precursors of slope instabilities. Two drone flight campaigns carried out one year apart, along with satellite-based interferometric analysis, served this purpose by highlighting processes of intense and persistent denudation of the slopes of interest in the study areas.

In the Paonia 1A area, signs of erosion phenomena mainly related to surface and concentrated runoff dynamics are clearly visible in both sectors. In the central parts, the presence of vegetation indicates an accumulation or stagnation of water and, specifically for Sector I, it is located just downstream from what appears to be a slight concavity in the stratification, well recognizable from the thermal image (Figure 4b). Sediment accumulation processes occur in these concentrated runoff rills and lead to the formation of diffuse (Figure 5c) or fan-shaped (Figure 4c) debris accretion, defined by an increase in height values in the change detection analysis. Due to this considerable sediment production, the maintenance activities, such as the accumulated debris removal, are particularly noticeable, as shown by the blue band in Figures 4c and 5c, indicating a decrease in elevation between 2021 and 2022. However, a minor part of this decrease is to be addressed to the vegetation changes between September 2021 (when the foot of the slope was covered by both living and dead vegetation) and June 2022. While in Sector I, the denudation processes seem to affect only the slope, in Sector II, we observe a more mature scenario of water erosion and infiltration that has led to the road surface's initial disruption. The micro-scale geomorphic features, both anthropic and natural, were pointed out by the change detection performed with IRIS software v. 23.0 (Figure 5d). Rills and gullies, formed after the precipitation event occurred on 19th September [72], identify the area most prone to degradation. Moreover, a wide convex road crack is the morphological evidence of this severe and persistent erosion that would possibly cause the partial failure of the highway. In this case in particular, but also for Sector I, the multispectral analysis is proof of how the slope is influenced by differential moisture conditions, which stand out immediately thanks to the presence of vegetation.

For the Paonia 1B area of interest, the results of the InSAR analysis (Figure 6) provided substantial information to study displacements occurring at the catchment scale and contribute to understanding the large-scale morpho-evolution of this area. Displacement values recorded by the PS confirm those from [70], delineating a complex scenario where the evolution of the Central East Muddy Creek Landslide Complex is highly interconnected to the opposite slope's instability asset and fluvial incision. The Central Landslide, due to its differential displacement pattern and annual velocity rates, still represents a critical condition for the risk assessment of SH133. Its activity style, characterized by discontinuous reactivation phases [70], defines a major threat to Colorado State Highway 133 (already damaged in 1986–1987). However, investigating this phenomenon, including its interaction with fluvial incision rate and mass-wasting processes on the opposite slope, would have required a proper modelization and was therefore not extensively carried out since it goes beyond the specific purpose of this work. On the other hand, the point measurements forming a cluster on the Paonia 1B slope of interest led to the identification of localized instabilities (Figure 9a). The movement can be correlated with unconsolidated materials sliding along the slope and then aligning in debris fans (clearly visible in the thermal product, Figure 9b) right below the PS cluster. This consistent waste deposit supply resulted in the complete occlusion of a drainage ditch (increase in height, Figure 9c), eventually cleaned during maintenance work (decrease in height, Figure 9c). As for the other study site, a clear example of the effects of intense denudation affecting specific portions of the hillslope is represented in the panels of Figure 8. Here, concentrated erosion processes drove the

disruption of the shotcrete applied for stabilizing the prominent banks. The shotcrete is abruptly interrupted in the southern part of the sandstone banks (Figure 8c), where a dense linear pattern of rills engraves the more erodible mudstone layers (Figure 8d,e). The Sector III example was provided to demonstrate the capacity of the sensors to identify not only the ongoing mass-wasting processes but also to point out early indicators of future instabilities. In this case, the multi-spectral information was essential to mark seeping areas where block detachment or collapses may easily occur (Figure 10).

The advantages of combining several sensors that could provide complementary information made it possible for an extensive investigation of different processes from a multi-scale perspective. Different landforms overlaying the slopes make it difficult to discern the corresponding process imprint and, therefore, to give a comprehensive representation of the territory's complexity [73]. Each of the applied sensors, with its specific spatial resolution, facilitated this task, enabling the extraction of one or more landform signatures and the relative forming process. Table 2 summarizes the scale of processes and related landforms detected through our multi-sensor approach. At the sub-catchment scale, the satellite-based InSAR analysis was the only medium-resolution technique that could measure the deformations with an accuracy comparable to the other methods. Gradually downscaling the investigation at the decametric and metric scales, thermal imagery and DEM-based analysis provided the most suitable results for delineating debris fans, blocks detached from the massive sandstone layers and areas subjected to concentrated runoff features. Eventually, micro-morphotypes were investigated by exploiting optical image-based change detection and multispectral classification. The micro-scale topographic landforms (i.e., road cracks and centimeter-scale rills) and subtle moisture variations (i.e., seep areas) respectively depicted by those methods can be correlated to early instability indicators. The regional-scale satellite-based products were effective in identifying possible areas of instability, while further downscaled investigations of those areas with drone-based high-resolution products provided significantly better outputs for the decision-making and mitigation processes of asset management plans. This multiscale approach was successful in identifying both the evidence and the early precursors of rock mass instability impacted by intense deterioration processes.

Table 2. Comparison between sensors, type of products and respective type of processes or landforms investigated at different scales.

Sensor	Type of Product	Scale	Type of Process or Landform
Satellite Radar (C band)	PS-InSAR analysis	Catchment or sub-catchment scale	Large landslides and deformations
Mavic 2 Pro integrated 20 mp	DEM-based change detection	Hillslope scale	Sediment accumulation and erosional processes
M2EA thermal	Thermal imagery	Hillslope scale	Humid zone and rock differentiation
Mavic 2 Pro integrated 20 mp	Optical imagery	Sub-hillslope scale	Small-scale topographic features
Mavic 2 Pro integrated 20 mp	Optical imagery-based change detection	Micro-topography scale	Rills and road crack formation or opening
Tetracam Micro-MCA6	Multispectral analysis	Sub-hillslope scale Micro-topography scale	Small-scale rock and soil differentiation Seep area identification

Although the combination of the aforementioned remote sensing techniques provided crucial insights into the slope deformation processes, some limitations in their applicability to our case study need to be considered. Despite the great advantage of free and open data, Sentinel C-band sensors are significantly affected by vegetation coverage, causing decorrelation issues that could reduce the quality of the interferometric measurements and

limit the accuracy and reliability of PS-InSAR for slope monitoring. Further improvements could be accomplished by employing sensors with longer wavelength characteristics (i.e., L-band sensors), better suited for monitoring slope movements in dense vegetation contexts due to their large penetration depths into canopies [74]. On the other hand, even if UAS-based data can be successfully employed for detecting and monitoring subtle or localized deformations, they are often impacted by weather and environmental conditions and can experience data processing challenges. Even slight illumination conditions can affect the reliability of thermic acquisition and optical analysis such as radiometric change detection, which in some cases faced shadowing issues. Therefore, well-planned UAS surveys are necessary (but not always easy to accomplish) for obtaining reliable results.

Within the framework of assessing rockfall hazards along transportation corridors, it is crucial to ensure the safety and functionality of these vital infrastructure networks. Debris and block detachments pose significant risks to motorists, leading to accidents, road closures, and costly maintenance operations. Transportation agencies are therefore tasked with identifying and prioritizing the most dangerous slopes that require immediate attention and allocation of resources. However, with extensive highway networks spanning vast areas, it becomes crucial for transportation agencies to adopt an effective yet rapid approach to evaluate and rank the hazardous slopes. The traditional field-based methods, while reliable, can be time-consuming, labor-intensive, and often limited in scope. In the current trend of implementing identification and rating systems for slopes affected by instability along infrastructures, previous studies [39–46] have predominantly focused on characterizing local-scale discontinuities within rock masses. The recognition and characterization of families of discontinuities, extensively studied in the literature, are necessary to understand the potential kinematics of block or debris detachment. However, it is fundamental to recognize that these factors alone are not the sole contributors predisposing a slope to collapse. Fluctuations in the temperature and water content, as well as the differential erosion affecting the sandstone and siltstone alternation, influence the weathering of rock slopes [75,76]. In this context, our study addresses the pressing need for an improved and replicable methodology that takes advantage of remote sensing data to facilitate the rapid quantification of those factors influencing rock mass stability. The approach employed in our study demonstrates that combining various remote sensing techniques enhances the identification of geomorphic processes and their impacts at different spatial scales. These outcomes provide valuable and practical insights that can be considered by transportation agencies when ranking slopes and assessing rockfall hazards through rockfall hazard rating systems (RHRS) [77]. The rationale of this engineering procedure is to classify high-risk slopes along transportation corridors, assigning a score based on several criteria, including factors such as ditch effectiveness, differential erosion rates and water presence. The traditional field-based RHRS encounters limitations due to time-consuming on-field measurements and potential underestimation of these factors, often addressed qualitatively. These limitations arise from restricted view angles, challenges in accessing certain sections of near-vertical or highly inclined slope surfaces, and the difficulty of investigating parameters at different scales while achieving a comprehensive understanding of the interconnected degradational processes [78]. With its multiscale, remotely sensed perspective, our study highlights the significance of providing a methodical and repeatable procedure to be implemented in the current rating systems for monitoring the sites and updating the assigned rating considering the spatio-temporal morphoevolution of the slope conditions. Furthermore, it takes into account the spatial variability and influence of pre-failure factors by employing different sensors and processing analyses.

6. Conclusions

Due to the mountainous topography of Colorado, much of the State Highway network has been developed through cut slopes. Along with predisposing factors such as the lithological asset and the road cuts, denudation processes play a fundamental role in destabilizing the unconsolidated material and the deterioration of the exposed rocks.

The investigation approach adopted in the present work succeeded in efficiently detecting the instabilities affecting the two slopes of interest along the Colorado SH133. In particular, the key findings of our work can be summarized as follows:

1. The combination of different platforms (satellite or UAS) and sensors, along with their respective products at varying spatial resolutions, was essential to identify several superimposed processes. Each informative level (i.e., multispectral and SAR analysis, thermal and optical products, terrain models), enabled distinguishing the specific geomorphic expression of the different degradation processes. In doing so, we shed light on the landform's multi-scale characteristics, thus interpreting their potential to differentially disrupt the slope stability. Moreover, the examples of retrogressive erosion and rill initiation retrieved in both study areas represent early predictors of future rock failures or road collapses.
2. The fourth dimension (i.e., time), explored through the use of multi-temporal data collections, provides a significant amplification of the potential of a single remote sensing survey. Change detection and interferometric analyses allowed the quantitative assessment of the dynamics of morphological features (e.g., road crack propagation, areas more susceptible to depletion or sediment accumulation) and a preliminary forecast of their morphoevolution.
3. Unusual processing solutions, such as optical-based change detection, can lead to new opportunities for micro-morphotype detection and characterization. This technique could serve as a primary step for a more quantitative assessment of the slope erosion rates and geostructural stability.
4. Remote sensing data can provide a detailed model of the slope's mechanics and conditions at a specific time. This information is particularly beneficial for monitoring highway networks and transportation corridors, supporting asset management practices from a predictive maintenance perspective.

Author Contributions: Conceptualization: T.O., P.M., B.T. and C.B.; Formal analysis: M.Z., A.K.K., A.J., C.C., R.D., D.V.H. and R.M.; Funding acquisition: B.T. and C.B.; Investigation: M.Z., A.K.K., A.J., C.C., R.D. and D.V.H.; Methodology: C.C. and R.D.; Project administration: T.O. and C.B.; Resources: T.O., B.T. and C.B.; Software: C.C. and R.D.; Supervision: T.O., F.T., P.M. and C.B.; Visualization: M.Z., A.K.K., A.J., C.C., D.V.H. and R.M.; Writing—original draft: M.Z., A.K.K. and C.C.; Writing—review and editing: T.O., F.T., P.M., B.T. and C.B. All authors have read and agreed to the published version of the manuscript.

Funding: This research was funded by the Colorado Department of Transportation, Geohazards Program, project number C SW02-479 (23706).

Data Availability Statement: Data results have been shared with the Colorado Department of Transportation (CDOT) Geohazards Program and can be available on request through the Corresponding Author with approval of CDOT.

Acknowledgments: The authors wish to thank Jordan Ewing and Abdul Rashid Zakaria for their valuable support during the field operations, and Antonio Cosentino for providing technical tips on the change detection analysis. We would also like to thank Robert Group at CDOT, and Ty Ortiz formerly of CDOT, for their roles in supporting the project.

Conflicts of Interest: The authors declare no conflict of interest.

References

1. Agliardi, F.; Crosta, G.B. High resolution three-dimensional numerical modelling of rockfalls. *Int. J. Rock Mech. Min. Sci.* **2003**, *40*, 455–471. [[CrossRef](#)]
2. Martino, S.; Bozzano, F.; Caporossi, P.; D'angiò, D.; Della Seta, M.; Esposito, C.; Fantini, A.; Fiorucci, M.; Giannini, L.M.; Iannucci, R.; et al. Impact of landslides on transportation routes during the 2016–2017 Central Italy seismic sequence. *Landslides* **2019**, *16*, 1221–1241. [[CrossRef](#)]
3. Landslides 101 | U.S. Geological Survey. Available online: <https://www.usgs.gov/programs/landslide-hazards/landslides-101> (accessed on 20 March 2023).

4. Lato, M.J.; Gauthier, D.; Hutchinson, D.J. Rock Slopes Asset Management: Selecting the Optimal Three-Dimensional Remote Sensing Technology. *Transp. Res. Rec.* **2015**, *2510*, 7–14. [[CrossRef](#)]
5. Arpin, B.; Arndt, B. Comparison of 2D and 3D rockfall modeling for rockfall mitigation design. In Proceedings of the 67th Highway Geology Symposium, Highway Geology Symposium, Colorado Springs, CO, USA, 11–14 July 2016.
6. Guzzetti, F. Landslide fatalities and the evaluation of landslide risk in Italy. *Eng. Geol.* **2000**, *58*, 89–107. [[CrossRef](#)]
7. Crosta, G.B.; Agliardi, F. A methodology for physically based rockfall hazard assessment. *Nat. Hazards Earth Syst. Sci.* **2003**, *3*, 407–422. [[CrossRef](#)]
8. Piacentini, D.; Ercolessi, G.; Pizziolo, M.; Troiani, F. Rockfall runout, Mount Cimone area, Emilia-Romagna Region, Italy. *J. Maps* **2015**, *11*, 598–605. [[CrossRef](#)]
9. Moore, J.R.; Sanders, J.W.; Dietrich, W.E.; Glaser, S.D. Influence of rock mass strength on the erosion rate of alpine cliffs. *Earth Surf. Process. Landf.* **2009**, *34*, 1339–1352. [[CrossRef](#)]
10. Karir, D.; Ray, A.; Bharati, A.K.; Chaturvedi, U.; Rai, R.; Khandelwal, M. Stability prediction of a natural and man-made slope using various machine learning algorithms. *Transp. Geotech.* **2022**, *34*, 100745. [[CrossRef](#)]
11. Khorram, S.; Nelson, S.A.; Koch, F.H.; van der Wiele, C.F. *Remote Sensing*; Springer Science & Business Media: Berlin/Heidelberg, Germany, 2012. [[CrossRef](#)]
12. Rosi, A.; Tofani, V.; Tanteri, L.; Tacconi Stefanelli, C.; Agostini, A.; Catani, F.; Casagli, N. The new landslide inventory of Tuscany (Italy) updated with PS-InSAR: Geomorphological features and landslide distribution. *Landslides* **2018**, *15*, 5–19. [[CrossRef](#)]
13. Dini, B.; Manconi, A.; Loew, S. Investigation of slope instabilities in NW Bhutan as derived from systematic DInSAR analyses. *Eng. Geol.* **2019**, *259*, 105111. [[CrossRef](#)]
14. Hussain, M.A.; Chen, Z.; Wang, R.; Shoaib, M. PS-InSAR-Based Validated Landslide Susceptibility Mapping along Karakoram Highway, Pakistan. *Remote Sens.* **2021**, *13*, 4129. [[CrossRef](#)]
15. Yuan, R.; Chen, J. A hybrid deep learning method for landslide susceptibility analysis with the application of InSAR data. *Nat. Hazards* **2022**, *114*, 1393–1426. [[CrossRef](#)]
16. Lucieer, A.; Jong, S.M.D.; Turner, D. Mapping landslide displacements using Structure from Motion (SfM) and image correlation of multi-temporal UAV photography. *Prog. Phys. Geogr.* **2013**, *38*, 97–116. [[CrossRef](#)]
17. Wang, W.; Zhao, W.; Chai, B.; Du, J.; Tang, L.; Yi, X. Discontinuity interpretation and identification of potential rockfalls for high-steep slopes based on UAV nap-of-the-object photogrammetry. *Comput. Geosci.* **2022**, *166*, 105191. [[CrossRef](#)]
18. Ismail, A.; Rashid, A.A.S.; Sa'ari, R.; Rasib, A.W.; Mustaffar, M.; Abdullah, R.A.; Kassim, A.; Mohd Yusof, N.; Abd Rahaman, N.; Mohd Apani, N.; et al. Application of UAV-based photogrammetry and normalised water index (NDWI) to estimate the rock mass rating (RMR): A case study. *Phys. Chem. Earth Parts A/B/C* **2022**, *127*, 103161. [[CrossRef](#)]
19. Filice, F.; Pezzo, A.; Lollino, P.; Perrotti, M.; Ietto, F. Multi-approach for the assessment of rock slope stability using in-field and UAV investigations. *Bull. Eng. Geol. Environ.* **2022**, *81*, 502. [[CrossRef](#)]
20. Robiati, C.; Eyre, M.; Vanneschi, C.; Francioni, M.; Venn, A.; Coggan, J. Application of Remote Sensing Data for Evaluation of Rockfall Potential within a Quarry Slope. *ISPRS Int. J. Geo-Inf.* **2019**, *8*, 367. [[CrossRef](#)]
21. Stead, D.; Donati, D.; Wolter, A.; Sturzenegger, M. Application of Remote Sensing to the Investigation of Rock Slopes: Experience Gained and Lessons Learned. *ISPRS Int. J. Geo-Inf.* **2019**, *8*, 296. [[CrossRef](#)]
22. Devoto, S.; Macovaz, V.; Mantovani, M.; Soldati, M.; Furlani, S. Advantages of Using UAV Digital Photogrammetry in the Study of Slow-Moving Coastal Landslides. *Remote Sens.* **2020**, *12*, 3566. [[CrossRef](#)]
23. Ismail, A.; Ahmad Safuan, A.R.; Sa'ari, R.; Wahid Rasib, A.; Mustaffar, M.; Asnida Abdullah, R.; Kassim, A.; Mohd Yusof, N.; Abd Rahaman, N.; Kalatehjari, R. Application of combined terrestrial laser scanning and unmanned aerial vehicle digital photogrammetry method in high rock slope stability analysis: A case study. *Meas. J. Int. Meas. Confed.* **2022**, *195*, 111161. [[CrossRef](#)]
24. Gantimurova, S.; Parshin, A.; Erofeev, V. GIS-Based Landslide Susceptibility Mapping of the Circum-Baikal Railway in Russia Using UAV Data. *Remote Sens.* **2021**, *13*, 3629. [[CrossRef](#)]
25. Konstantinidis, I.; Marinos, V.; Papathanassiou, G. UAV-Based Evaluation of Rockfall Hazard in the Cultural Heritage Area of Kipinas Monastery, Greece. *Appl. Sci.* **2021**, *11*, 8946. [[CrossRef](#)]
26. Udin, W.S.; Norazami, N.A.S.; Sulaiman, N.; Zaudin, N.C.; Ma'ail, S.; Nor, A.M. UAV based multi-spectral imaging system for mapping landslide risk area along Jeli-Gerik highway, Jeli, Kelantan. In Proceedings of the 2019 IEEE 15th International Colloquium on Signal Processing & Its Applications (CSPA), Pulau Pinang, Malaysia, 8–9 March 2019; pp. 162–167. [[CrossRef](#)]
27. Wang, S.; Zhang, Z.; Wang, C.; Zhu, C.; Ren, Y. Multistep rocky slope stability analysis based on unmanned aerial vehicle photogrammetry. *Environ. Earth Sci.* **2019**, *78*, 260. [[CrossRef](#)]
28. Robiati, C.; Mastrantoni, G.; Francioni, M.; Eyre, M.; Coggan, J.; Mazzanti, P. Contribution of High-Resolution Virtual Outcrop Models for the Definition of Rockfall Activity and Associated Hazard Modelling. *Land* **2023**, *12*, 191. [[CrossRef](#)]
29. Lin, J.; Wang, M.; Yang, J.; Yang, Q. Landslide identification and information extraction based on optical and multispectral UAV remote sensing imagery. In *IOP Conference Series: Earth and Environmental Science*; IOP Publishing: Beijing, China, 2016; Volume 57, p. 012017.
30. He, J.; Barton, I. Hyperspectral remote sensing for detecting geotechnical problems at Ray mine. *Eng. Geol.* **2019**, *292*, 106261. [[CrossRef](#)]

31. Frodella, W.; Gigli, G.; Morelli, S.; Lombardi, L.; Casagli, N. Landslide Mapping and Characterization through Infrared Thermography (IRT): Suggestions for a Methodological Approach from Some Case Studies. *Remote Sens.* **2017**, *9*, 1281. [[CrossRef](#)]
32. Abellán, A.; Calvet, J.; Vilaplana, J.M.; Blanchard, J. Detection and spatial prediction of rockfalls by means of terrestrial laser scanner monitoring. *Geomorphology* **2010**, *119*, 162–171. [[CrossRef](#)]
33. Royán, M.J.; Abellán, A.; Jaboyedoff, M.; Vilaplana, J.M.; Calvet, J. Spatio-temporal analysis of rockfall pre-failure deformation using Terrestrial LiDAR. *Landslides* **2014**, *11*, 697–709. [[CrossRef](#)]
34. Kromer, R.A.; Hutchinson, D.J.; Lato, M.J.; Gauthier, D.; Edwards, T. Identifying rock slope failure precursors using LiDAR for transportation corridor hazard management. *Eng. Geol.* **2015**, *195*, 93–103. [[CrossRef](#)]
35. Farmakis, I.; Marinos, V.; Papathanassiou, G.; Karantanellis, E. Automated 3D Jointed Rock Mass Structural Analysis and Characterization Using LiDAR Terrestrial Laser Scanner for Rockfall Susceptibility Assessment: Perissa Area Case (Santorini). *Geotech. Geol. Eng.* **2020**, *38*, 3007–3024. [[CrossRef](#)]
36. Núñez-Andrés, M.A.; Prades-Valls, A.; Matas, G.; Buill, F.; Lantada, N. New Approach for Photogrammetric Rock Slope Premonitory Movements Monitoring. *Remote Sens.* **2023**, *15*, 293. [[CrossRef](#)]
37. Carlà, T.; Nolesini, T.; Solari, L.; Rivolta, C.; Dei Cas, L.; Casagli, N. Rockfall forecasting and risk management along a major transportation corridor in the Alps through ground-based radar interferometry. *Landslides* **2019**, *16*, 1425–1435. [[CrossRef](#)]
38. Romeo, S.; Cosentino, A.; Giani, F.; Mastrantoni, G.; Mazzanti, P. Combining Ground Based Remote Sensing Tools for Rockfalls Assessment and Monitoring: The Poggio Baldi Landslide Natural Laboratory. *Sensors* **2021**, *21*, 2632. [[CrossRef](#)]
39. Graber, A.; Santi, P. UAV-photogrammetry rockfall monitoring of natural slopes in Glenwood Canyon, CO, USA: Background activity and post-wildfire impacts. *Landslides* **2023**, *20*, 229–248. [[CrossRef](#)]
40. Sarro, R.; Riquelme, A.; García-Davalillo, J.C.; Mateos, R.M.; Tomás, R.; Pastor, J.L.; Herrera, G. Rockfall Simulation Based on UAV Photogrammetry Data Obtained during an Emergency Declaration: Application at a Cultural Heritage Site. *Remote Sens.* **2018**, *10*, 1923. [[CrossRef](#)]
41. Francioni, M.; Antonaci, F.; Sciarra, N.; Robiati, C.; Coggan, J.; Stead, D.; Calamita, F. Application of Unmanned Aerial Vehicle Data and Discrete Fracture Network Models for Improved Rockfall Simulations. *Remote Sens.* **2020**, *12*, 2053. [[CrossRef](#)]
42. Gallo, I.G.; Martínez-Corbella, M.; Sarro, R.; Iovine, G.; López-Vinielles, J.; Hernández, M.; Robustelli, G.; Mateos, R.M.; García-Davalillo, J.C. An Integration of UAV-Based Photogrammetry and 3D Modelling for Rockfall Hazard Assessment: The Cárcavos Case in 2018 (Spain). *Remote Sens.* **2021**, *13*, 3450. [[CrossRef](#)]
43. Žabota, B.; Berger, F.; Kobal, M. The Potential of UAV-Acquired Photogrammetric and LiDAR-Point Clouds for Obtaining Rock Dimensions as Input Parameters for Modeling Rockfall Runout Zones. *Drones* **2023**, *7*, 104. [[CrossRef](#)]
44. Migliazza, M.; Carriero, M.T.; Lingua, A.; Pontoglio, E.; Scavia, C. Rock Mass Characterization by UAV and Close-Range Photogrammetry: A Multiscale Approach Applied along the Vallone dell’Elva Road (Italy). *Geosciences* **2021**, *11*, 436. [[CrossRef](#)]
45. Rodriguez, J.; Macciotta, R.; Hendry, M.T.; Roustaei, M.; Gräpel, C.; Skirrow, R. UAVs for monitoring, investigation, and mitigation design of a rock slope with multiple failure mechanisms—A case study. *Landslides* **2020**, *17*, 2027–2040. [[CrossRef](#)]
46. Caliò, D.; Mineo, S.; Pappalardo, G. Digital Rock Mass Analysis for the Evaluation of Rockfall Magnitude at Poorly Accessible Cliffs. *Remote Sens.* **2023**, *15*, 1515. [[CrossRef](#)]
47. Liu, Z.; Qiu, H.; Ma, S.; Yang, D.; Pei, Y.; Du, C.; Sun, H.; Hu, S.; Zhu, Y. Surface displacement and topographic change analysis of the Changhe landslide on September 14, 2019, China. *Landslides* **2021**, *18*, 1471–1483. [[CrossRef](#)]
48. Ma, S.; Qiu, H.; Hu, S.; Yang, D.; Liu, Z. Characteristics and geomorphology change detection analysis of the Jiangdingya landslide on July 12, 2018, China. *Landslides* **2021**, *18*, 383–396. [[CrossRef](#)]
49. Hu, S.; Qiu, H.; Wang, N.; Wang, X.; Ma, S.; Yang, D.; Wei, N.; Liu, Z.; Shen, Y.; Cao, M.; et al. Movement process, geomorphological changes, and influencing factors of a reactivated loess landslide on the right bank of the middle of the Yellow River, China. *Landslides* **2022**, *19*, 1265–1295. [[CrossRef](#)]
50. Liu, Z.; Qiu, H.; Zhu, Y.; Liu, Y.; Yang, D.; Ma, S.; Zhang, J.; Wang, Y.; Wang, L.; Tang, B. Efficient Identification and Monitoring of Landslides by Time-Series InSAR Combining Single- and Multi-Look Phases. *Remote Sens.* **2022**, *14*, 1026. [[CrossRef](#)]
51. Johnson, R.C.; May, F. A study of the Cretaceous-Tertiary unconformity in the Piceance Creek Basin, Colorado: The underlying Ohio Creek Formation (Upper Cretaceous) redefined as a member of the Hunter Canyon or Mesaverde Formation. *Geol. Surv. Bull.* **1980**, 1482-B.
52. Godwin, L.H. *Geologic Map of the Chair Mountain Quadrangle, Gunnison and Pitkin Counties, Colorado*; (No. 704); USGA: Reston, VA, USA, 1968. [[CrossRef](#)]
53. Johnson, R.C. *Geologic History and Hydrocarbon Potential of Late Cretaceous-Age, Low-Permeability Reservoirs, Piceance Basin, Western Colorado*; (No. 1787-E); USGA: Reston, VA, USA, 1989. [[CrossRef](#)]
54. Dunrud, C.R. *Geologic Map and Coal Stratigraphic Framework of the Paonia Area, Delta and Gunnison Counties, Colorado*; (No. 115); USGA: Reston, VA, USA, 1989. [[CrossRef](#)]
55. Aswathi, J.; Binoj Kumar, R.B.; Oommen, T.; Bouali, E.H.; Sajinkumar, K.S. InSAR as a tool for monitoring hydropower projects: A review. *Energy Geosci.* **2022**, *3*, 160–171. [[CrossRef](#)]
56. Ferretti, A.; Prati, C.; Rocca, F. Permanent scatterers in SAR interferometry. *IEEE Trans. Geosci. Remote Sens.* **2001**, *39*, 8–20. [[CrossRef](#)]
57. Funning, G.J.; Bürgmann, R.; Ferretti, A.; Novali, F.; Fumagalli, A. Creep on the Rodgers Creek fault, northern San Francisco Bay area from a 10 year PS-InSAR dataset. *Geophys. Res. Lett.* **2007**, *34*. [[CrossRef](#)]

58. Perissin, D.; Wang, Z.; Wang, T. The SARPROZ InSAR tool for urban subsidence/manmade structure stability monitoring in China. In Proceedings of the 34th International Symposium of Remote Sensing of Environment, Sidney, Australia, 10–15 April 2011.
59. Antonielli, B.; Sciortino, A.; Scancella, S.; Bozzano, F.; Mazzanti, P. Tracking Deformation Processes at the Legnica Glogow Copper District (Poland) by Satellite InSAR—I: Room and Pillar Mine District. *Land* **2021**, *10*, 653. [[CrossRef](#)]
60. Moretto, S.; Bozzano, F.; Mazzanti, P. The Role of Satellite InSAR for Landslide Forecasting: Limitations and Openings. *Remote Sens.* **2021**, *13*, 3735. [[CrossRef](#)]
61. Trimble Germany GmbH. *Trimble Documentation eCognition Developer 10.1 User Guide*; Trimble Germany GmbH: Munich, Germany, 2022.
62. Blaschke, T. Object based image analysis for remote sensing. *ISPRS J. Photogramm. Remote Sens.* **2010**, *65*, 2–16. [[CrossRef](#)]
63. Hussain, M.; Chen, D.; Cheng, A.; Wei, H.; Stanley, D. Change detection from remotely sensed images: From pixel-based to object-based approaches. *ISPRS J. Photogramm. Remote Sens.* **2013**, *80*, 91–106. [[CrossRef](#)]
64. Asokan, A.; Anitha, J.J.E.S.I. Change detection techniques for remote sensing applications: A survey. *Earth Sci. Inform.* **2019**, *12*, 143–160. [[CrossRef](#)]
65. Photomonitoring.com. Available online: <https://www.photomonitoring.com/iris/> (accessed on 25 April 2023).
66. Wang, Z.; Bovik, A.C.; Sheikh, H.R.; Simoncelli, E.P. Image Quality Assessment: From Error Visibility to Structural Similarity. *IEEE Trans. Image Process.* **2004**, *13*, 600–612. [[CrossRef](#)]
67. Cosentino, A.; Brunetti, A.; Fiorio, M.; Gaeta, M.; Mazzanti, P. IRIS a new powerful tool for Geohazards Assessment by PhotoMonitoring. In Proceedings of the Asita Conference, Genova, Italy, 20–24 June 2022.
68. Mazzanti, P.; Scancella, S.; Virelli, M.; Frittelli, S.; Nocente, V.; Lombardo, F. Assessing the Performance of Multi-Resolution Satellite SAR Images for Post-Earthquake Damage Detection and Mapping Aimed at Emergency Response Management. *Remote Sens.* **2022**, *14*, 2210. [[CrossRef](#)]
69. Stover, B.K. *Surficial-Geologic Map of the Muddy Creek Landslide Complex, Gunnison County, Colorado, April 15, 1986*; Surface Geologic, Open File Report; Colorado Geological Survey, Department of Natural Resources: Denver, CO, USA, 1986. Available online: <https://coloradogeologicalsurvey.org/publications/surficial-geologic-map-muddy-creek-landslide-complex-gunnison-colorado-1986/> (accessed on 6 June 2023).
70. Lowry, B.W.; Baker, S.; Zhou, W. A Case Study of Novel Landslide Activity Recognition Using ALOS-1 InSAR within the Ragged Mountain Western Hillslope in Gunnison County, Colorado, USA. *Remote Sens.* **2020**, *12*, 1969. [[CrossRef](#)]
71. U.S. Geological Survey. 3D Elevation Program 1-Meter Resolution Digital Elevation Model (Published 20200606). 2019. Available online: <https://www.usgs.gov/the-national-map-data-delivery> (accessed on 24 April 2023).
72. Weatherwx.com. Available online: <https://www.weatherwx.com/climate-averages/co/paonia+reservoir.html> (accessed on 24 April 2023).
73. Schmidt, J.; Andrew, R. Multi-scale landform characterization. *Area* **2005**, *37*, 341–350. [[CrossRef](#)]
74. El Hajj, M.; Baghdadi, N.; Zribi, M. Comparative analysis of the accuracy of surface soil moisture estimation from the C- and L-bands. *Int. J. Appl. Earth Obs. Geoinf.* **2019**, *82*, 101888. [[CrossRef](#)]
75. Draebing, D. Identification of rock and fracture kinematics in high alpine rockwalls under the influence of elevation. *Earth Surf. Dyn.* **2021**, *9*, 977–994. [[CrossRef](#)]
76. Birien, T.; Gauthier, F. Influence of climate-dependent variables on deformation and differential erosion of stratified sedimentary rocks. *Geomorphology* **2023**, *421*, 108518. [[CrossRef](#)]
77. Santi, P.M.; Russell, C.P.; Higgins, J.D.; Spriet, J.I. Modification and statistical analysis of the Colorado Rockfall Hazard Rating System. *Eng. Geol.* **2009**, *104*, 55–65. [[CrossRef](#)]
78. Oommen, T.; Vitton, S.; Escobar-Wolf, R.; Brooks, C. Rockfall Hazard Rating System: Benefits of Utilizing Remote Sensing. *Environ. Eng. Geosci.* **2017**, *23*, 165–177. [[CrossRef](#)]

Disclaimer/Publisher’s Note: The statements, opinions and data contained in all publications are solely those of the individual author(s) and contributor(s) and not of MDPI and/or the editor(s). MDPI and/or the editor(s) disclaim responsibility for any injury to people or property resulting from any ideas, methods, instructions or products referred to in the content.